ORIGINAL ARTICLE

lajss.org© Latin American Journal of Solids and Structures

www.lajss.org

Analytical and experimental study on elliptical cross-section double-ogive-nose projectile penetration into plain concrete target

Xianghui Dai[a]*, Kehui Wang[a], Gang Zhou[a], Zikai Shen[a], Ming Ke[a], Ming Li[a]

[a] Laboratory of Intense Dynamic Loading and Effect, Northwest Institute of Nuclear Technology, Xi'an, Shaanxi 710024, P R China.
E-mails: daixianghui@nint.ac.cn, wangkehui@nint.ac.cn, gzhou@nint.ac.cn, shenzikai@nint.ac.cn, keming@nint.ac.cn, liming@nint.ac.cn

* Corresponding author

https://doi.org/10.1590/1679-78257753

Abstract

A general geometric model of the elliptical cross-section double-ogive-nose projectile (ECDP) was established, and the expression of penetration resistance was obtained. Based on the special shape and penetration process characteristics of the ECDP, a three-stage penetration model was constructed, and closed-form penetration equations were derived. Three ECDPs with the major–minor axis ratio of 1.5 were launched by a 130 mm gas-gun to impact the plain concrete targets with the oblique angle of 10° at a nominal striking velocity of 650 m/s, the experimental data such as the penetration depth of the ECDPs and the failure characteristic parameter of the targets was obtained. The initial posture of the ECDP had little effect on the penetration depth and trajectory deflection under the condition of the target with 10° oblique angle, but it had obvious influence on the structural response. The theoretical model was verified by experimental data, the calculated result of the penetration depth was in good agreement with the experimental data, the deviation was within the range of -13.5% ~ -8.5%.

Keywords

Projectile, Penetration, Concrete target, Elliptical cross-section, Double-ogive-nose.

Graphical Abstract

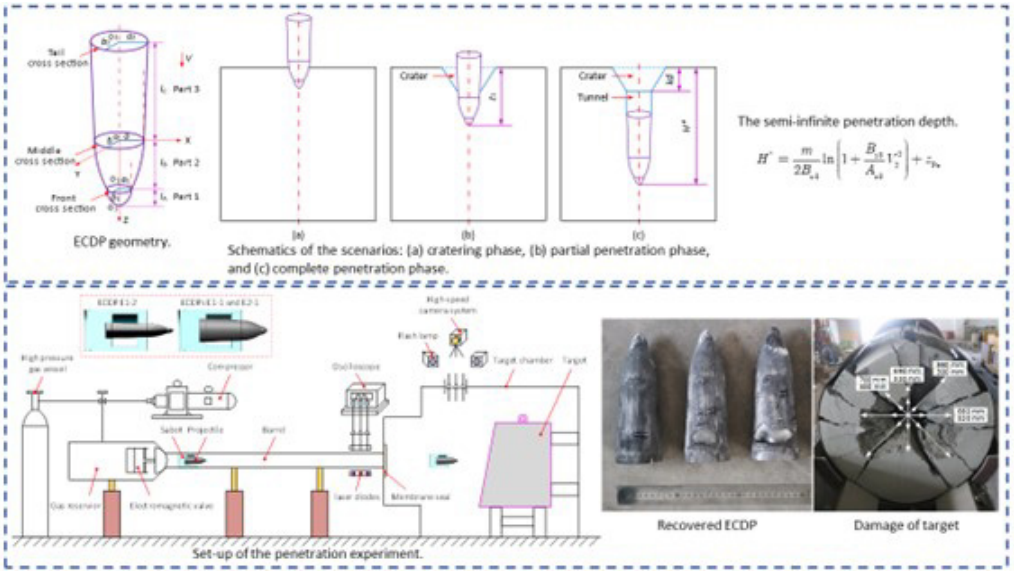

Received: June 30, 2023. In revised form: November 02, 2023. Accepted: December 15, 2023. Available online: January 16, 2024.
https://doi.org/10.1590/1679-78257753

1 INTRODUCTION

The hypersonic weapon is an effective way to attack the deep underground targets in the future. In order to improve the lift-drag ratio of the hypersonic weapon in flight, the waverider configuration is gradually adopted. Due to the need of space layout, the projectile installation space of the hypersonic weapon is also designed to be extremely irregular. In order to make full use of the flat and irregular installation space, the projectile is inclined to be designed into a heterotypic structure. Therefore, the research on the terminal ballistic effect of this special projectile has attracted the attention of scholars.

In recent years, the terminal ballistic effect of the elliptical cross-section single-ogive-nose projectile (ECSP) penetration into the plain concrete target has been studied. Dai et al. (2020, 2021) proposed the closed-form penetration formula of the ECSP based on the cavity-expansion theory, and discussed the penetration performance of the ECSP. Moreover, the penetration-depth increment of the ECSP was evaluated, and the influence of the major–minor axis ratio on the penetration-depth increment was discussed. Dong et al. (2019) conducted some experiments of the ECSP penetration into the plain concrete target, and the experimental result showed that the ECSP had excellent trajectory stability and penetration performance. Further, based on the assumption of the relationship between the normal velocity and the normal stress on the projectile nose surface, a theoretical model for calculating the penetration depth of the ECSP was proposed. Wu et al. (2023) established a three-dimensional trajectory model for an elliptical projectile into semi-infinite target based on rigid dynamics and the idea of isolation between the projectile and target, and discussed the influences of structural parameters and initial striking conditions of elliptical projectiles on trajectory stability.

Additionally, the terminal ballistic effect of the circular cross-section double-ogive-nose projectile (CCDP) penetration into the plain concrete target has also been studied recently. According to the dynamic cavity-expansion theory, Liu et al. (2015) discussed the influence of the nose shape on the penetration resistance, and presented an optimized design scheme of a CCDP with lesser penetration resistance. Zhang et al. (2017) carried out high-velocity penetration experiments. The CCDP and the circular cross-section ogive-nose projectile (CCOP) were used to perforate or penetrate concrete targets, and the experimental result showed that the CCDP had better penetration performance than the CCOP within a striking velocity range of 1000 m/s ~ 1360 m/s.

As mentioned above, great efforts have been contributed by the investigation about the terminal ballistic effect of the ECSP and CCDP, the corresponding theoretical model has been constructed and verified, and the advantage of the heterotypic projectile in some specific situations has been proved. At the same time, the more advanced elliptical cross-section double-ogive-nose projectile (ECDP), which combines the advantages of the ECSP and CCDP, gradually attracted the attention of weapon designers. However, the research on the ECDP penetration into concrete target has not been reported so far, and the theoretical model has not been established, which brings great inconvenience to the actual engineering design of the ECDP.

In the present study, the general geometric model of the ECDP is established, and the theoretical model of the ECDP penetration into semi-infinite plain concrete target is proposed. The experiments of the ECDP with the major–minor axis ratio of 1.5 penetration into plain concrete target are carried out. The validity of the theoretical model is verified by experimental data, and the reasons for the deviation are discussed.

2 THEORETICAL MODEL

In this section, based on our previous work (Dai et al. 2020; Dai et al. 2021), a semi-analytical formula is proposed to calculate the terminal ballistic parameters of the ECDP penetration into semi-infinite plain concrete target.

2.1 Geometry

Figure 1 shows the geometry of the ECDP. a and b represent the semi-major and the semi-minor axis of the middle cross-section ellipse, respectively. a_1 and b_1 represent the semi-major and the semi-minor axis of the front cross-section ellipse, respectively. a_2 and b_2 represent the semi-major and the semi-minor axis of the tail cross-section ellipse, respectively. l_A, l_B, and l_C represent the length of parts 1, 2, and 3, respectively. The ogival curve is an arc tangent to the parallel line of the projectile axis. The arrow indicates the penetration direction, and V represents the instantaneous penetration velocity.

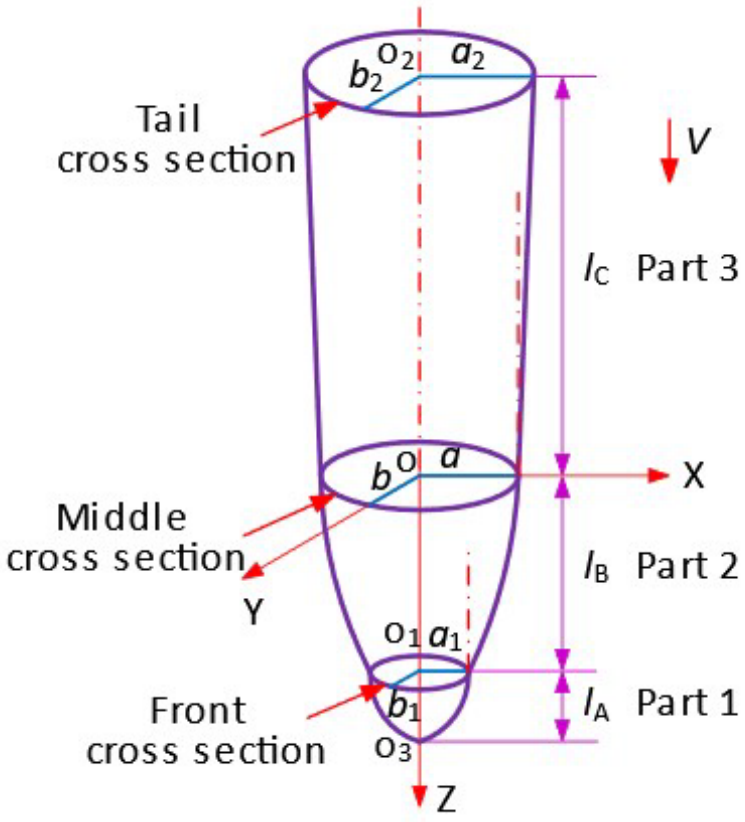

Figure 1 ECDP geometry.

2.2 Resistance

Several formulas have been proposed to predict the axial resistance of the ECSPs penetration into the semi-infinite concrete targets (Dai et al. 2020; Dai et al. 2021). In the present study, parts 1, 2, and 3 can be considered as ogival nose, truncated ogival nose, and truncated conical nose of the ECSPs, respectively. Therefore, the axial resistance F_n for each part takes the form shown in Eq. (1) during the tunneling process.

$$F_n = A_n + B_n V^2 \tag{1}$$

In Eq. (1), A_n refers to the static resistance, and B_n refers to the dynamic resistance coefficient. Further, the subscript "n" represents the different parts of the ECDP. From Dai et al. (2020), A_n and B_n are obtained as shown in Eq. (2).

$$A_1 = Ra_1b_1\int_0^{2\pi}\int_0^1 \frac{2\left(1-\rho\right)^{1/2} l_1}{\left\{\frac{\cos^2\alpha\left[2a_1^2\left(\rho-1\right)+l_1^2\right]^2}{a_1^2}+\frac{\sin^2\alpha\left[2b_1^2\left(\rho-1\right)+l_1^2\right]^2}{b_1^2}+4\left(1-\rho\right)l_1^2\right\}^{1/2}} \times\left\{1+\frac{1}{4\left(1-\rho\right)l_1^2}\left[\frac{\cos^2\alpha\left[2a_1^2\left(\rho-1\right)+l_1^2\right]^2}{a_1^2}+\frac{\sin^2\alpha\left[2b_1^2\left(\rho-1\right)+l_1^2\right]^2}{b_1^2}\right]\right\}^{1/2}\rho\mathrm{d}\rho\mathrm{d}\alpha \tag{2a}$$

$$B_1=\rho_t a_1 b_1\int_0^{2\pi}\int_0^1 \frac{8\left(1-\rho\right)^{3/2}l_1^3}{\left\{\frac{\cos^2\alpha\left[2a_1^2\left(\rho-1\right)+l_1^2\right]^2}{a_1^2}+\frac{\sin^2\alpha\left[2b_1^2\left(\rho-1\right)+l_1^2\right]^2}{b_1^2}+4\left(1-\rho\right)l_1^2\right\}^{3/2}} \times\left\{1+\frac{1}{4\left(1-\rho\right)l_1^2}\left[\frac{\cos^2\alpha\left[2a_1^2\left(\rho-1\right)+l_1^2\right]^2}{a_1^2}+\frac{\sin^2\alpha\left[2b_1^2\left(\rho-1\right)+l_1^2\right]^2}{b_1^2}\right]\right\}^{1/2}\rho\mathrm{d}\rho\mathrm{d}\alpha \tag{2b}$$

$$A_2=Rab\int_0^{2\pi}\int_{\frac{a_1}{a}}^1 \frac{2\left(1-\rho\right)^{1/2}l_2}{\left\{\frac{\cos^2\alpha\left[2a^2\left(\rho-1\right)+l_2^2\right]^2}{a^2}+\frac{\sin^2\alpha\left[2b^2\left(\rho-1\right)+l_2^2\right]^2}{b^2}+4\left(1-\rho\right)l_2^2\right\}^{1/2}} \times\left\{1+\frac{1}{4\left(1-\rho\right)l_2^2}\left[\frac{\cos^2\alpha\left[2a^2\left(\rho-1\right)+l_2^2\right]^2}{a^2}+\frac{\sin^2\alpha\left[2b^2\left(\rho-1\right)+l_2^2\right]^2}{b^2}\right]\right\}^{1/2}\rho\mathrm{d}\rho\mathrm{d}\alpha \tag{2c}$$

$$B_2=\rho_t ab\int_0^{2\pi}\int_{\frac{a_1}{a}}^1 \frac{8\left(1-\rho\right)^{3/2}l_2^3}{\left\{\frac{\cos^2\alpha\left[2a^2\left(\rho-1\right)+l_2^2\right]^2}{a^2}+\frac{\sin^2\alpha\left[2b^2\left(\rho-1\right)+l_2^2\right]^2}{b^2}+4\left(1-\rho\right)l_2^2\right\}^{3/2}} \times\left\{1+\frac{1}{4\left(1-\rho\right)l_2^2}\left[\frac{\cos^2\alpha\left[2a^2\left(\rho-1\right)+l_2^2\right]^2}{a^2}+\frac{\sin^2\alpha\left[2b^2\left(\rho-1\right)+l_2^2\right]^2}{b^2}\right]\right\}^{1/2}\rho\mathrm{d}\rho\mathrm{d}\alpha \tag{2d}$$

$$A_3=R\pi\left(a_2b_2-ab\right) \tag{2e}$$

$$B_3=\frac{1}{2}\rho_t\frac{\left(a_2^2-a^2\right)b_2}{a_2}\int_0^{2\pi}\frac{1}{l_{\mathrm{N2}}^2\left(\frac{\cos^2\alpha}{a_2^2}+\frac{\sin^2\alpha}{b_2^2}\right)+1}\mathrm{d}\alpha \tag{2f}$$

In Eq. (2), ρ and α are the polar coordinate transformation parameter (Dai et al. 2020), ρ_t and R represent the density and the resistance parameter of the concrete target, respectively. $R = Sf_c$ was first proposed by Frew et al. (1998), where f_c refers to the unconfined compressive strength of the concrete target, and S refers to the empirical constant of the concrete target, which is given by $S = 72.0f_c^{-0.5}$ and $S = 82.6f_c^{-0.544}$ (Frew et al. 1998; Li and Chen 2003). In this work, $S = 82.6f_c^{-0.544}$ is selected. Further, the length variables are expressed as shown in Eq. (3), they meanings as shown in Dai et al. (2020).

$$l_1=\sqrt{l_{\mathrm{A}}^2+a_1^2\rho\cos^2\alpha+b_1^2\rho\sin^2\alpha} \tag{3a}$$

$$l_2=\sqrt{l_{\mathrm{N1}}^2+a^2\rho\cos^2\alpha+b^2\rho\sin^2\alpha} \tag{3b}$$

$$l_{\mathrm{N1}} = \sqrt{\frac{a\left(l_{\mathrm{B}}^2 - aa_1 + a_1^2\right)}{a - a_1}} \tag{3c}$$

$$l_{\mathrm{N2}} = \frac{a_2 l_{\mathrm{C}}}{a_2 - a} \tag{3d}$$

As the ECDP has a conical shank, the penetration process is divided into three phases, namely, the cratering phase, the partial penetration phase, and the complete penetration phase, as shown in Figure 2. The total axial resistance expression of the ECDP is different in each penetration phase.

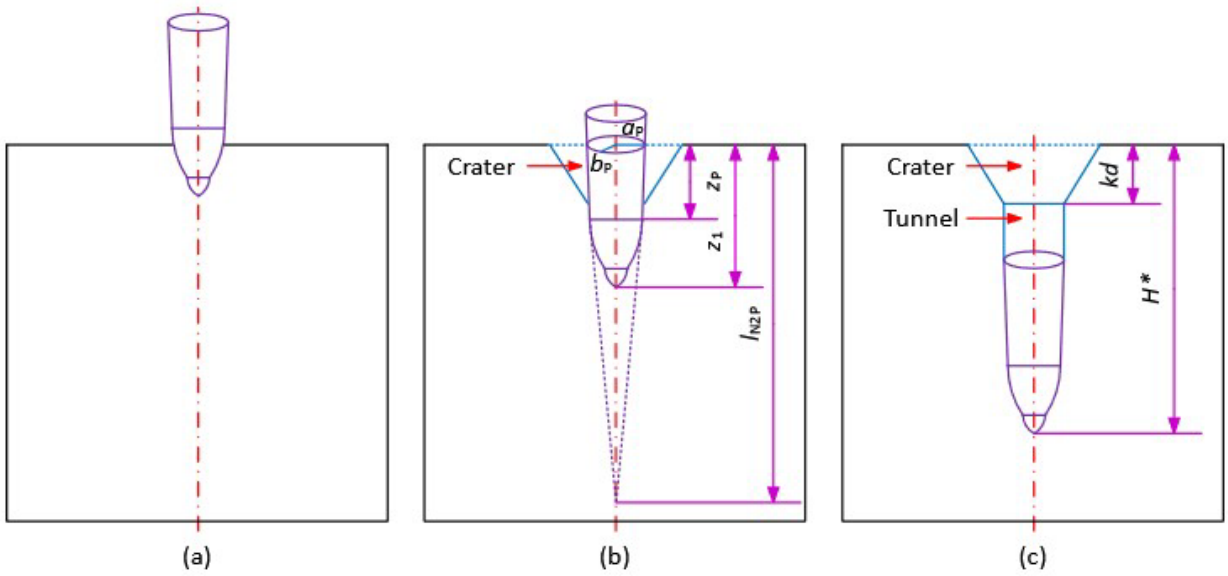

Figure 2 Schematics of the scenarios: (a) cratering phase, (b) partial penetration phase, and (c) complete penetration phase.

2.2.1. Penetration resistance of the double ogival nose

The axial resistance of the double ogival nose includes the ogival nose (Part 1) and the truncated ogival nose (Part 2), which is expressed as shown in Eq. (4).

$$F_{\mathrm{d}} = A_{\mathrm{d}} + B_{\mathrm{d}} V^2 \tag{4}$$

In Eq. (4),

$$A_{\mathrm{d}} = A_1 + A_2 \tag{5a}$$

$$B_{\mathrm{d}} = B_1 + B_2 \tag{5b}$$

2.2.2. Penetration resistance of the conical shank

(1) Partial penetration phase

By using the same method that was used for solving the axial resistance of the truncated-conical-nose projectile (Dai et al. 2020), the axial resistance of the projectile shank that has penetrated into the target is expressed as given in Eq. (6).

$$F_{\mathrm{3P}} = A_{\mathrm{3P}} + B_{\mathrm{3P}} V^2 \tag{6}$$

In Eq. (6), A_{3P} represent the static resistance and B_{3P} represent the dynamic resistance coefficient of the conical shank. They are given as Eq. (7).

$$A_{3P} = R\pi\left(a_P b_P - ab\right) \tag{7a}$$

$$B_{3P} = \frac{1}{2}\rho_t \frac{\left(a_P^2 - a^2\right)b_P}{a_P}\int_0^{2\pi} \frac{1}{l_{N2P}^2\left(\frac{\cos^2\alpha}{a_P^2} + \frac{\sin^2\alpha}{b_P^2}\right)+1}\mathrm{d}\alpha \tag{7b}$$

Further, the parameters a_P and b_P represent the semi-major axis and the semi-minor axis of the tail cross-section ellipse of the projectile shank that has penetrated into the target, respectively, and l_{N2P} represents the total length of the truncated conical shank that has penetrated into the target. They are expressed as given in Eq. (8).

$$a_P = \frac{z_P}{l_C}\left(a_2 - a\right) + a \tag{8a}$$

$$b_P = \frac{z_P}{l_C}\left(b_2 - b\right) + b \tag{8b}$$

$$l_{N2P} = \frac{a_P z_P}{a_P - a} \tag{8c}$$

In Eq. (8), z_P represents the length of the projectile shank that has penetrated into the target, i.e. $z_P = z_1 - l_A - l_B$, and z_1 represents the instantaneous penetration depth.

(2) Complete penetration phase

The axial resistance of the conical shank in the complete penetration phase is expressed as shown in Eq. (9).

$$F_3 = A_3 + B_3 V^2 \tag{9}$$

2.2.3. Penetration resistance of the ECDP

(1) Cratering phase

In the cratering phase, the axial resistance of the ECDP is given as Eq. (10) (Forrestal et al. 1994).

$$F_{z1} = c_1 z_1,\ 0 \le z_1 \le kd \tag{10}$$

In Eq. (10), c_1 is a constant, kd is the depth of the front crater, and d is the equivalent diameter of the middle cross-section ellipse. Moreover, k = 2.0 is selected in the present study.

Assuming that the double ogival nose penetrates completely into the target at the end of the cratering phase, the axial resistance of the ECDP is obtained as shown in Eq. (11).

$$F_{ze} = A_d + B_d V_1^2 \tag{11}$$

In Eq. (11), V_1 represents the instantaneous velocity of the ECDP at the end of the cratering phase.

(2) Partial penetration phase

In the partial penetration phase, the axial resistance of the ECDP is the sum of the axial resistance of the double ogival nose and the truncated conical shank that has penetrated into the target. It is expressed as Eq. (12).

$$F_{z2} = A_{z2} + B_{z2}V^2 \tag{12}$$

In Eq. (12),

$$A_{z2} = A_1 + A_2 + A_{3P} \tag{13a}$$

$$B_{z2} = B_1 + B_2 + B_{3P} \tag{13b}$$

Further, Eq. (12) is a nonlinear function of the instantaneous penetration velocity V and instantaneous penetration depth z_1. Therefore, there is no analytical solution to the penetration differential equation that was established by Newton's second law of motion. Furthermore, in order to obtain the analytical solution of the penetration differential equation, the method adopted in Teland and Sjol (2004) and Sun et al. (2010) is considered. Therefore, it is given as Eq. (14).

$$F_{z2} = F_{ze} + c_2\left(z_1 - kd\right) \tag{14}$$

In Eq. (14), c_2 is a constant.

(3) Complete penetration phase

In the complete penetration phase, the axial resistance of the ECDP is the sum of the axial resistance of the double ogival nose and the truncated conical shank, which is expressed as shown in Eq. (15).

$$F_{z3} = A_{z3} + B_{z3}V^2 \tag{15}$$

In Eq. (15),

$$A_{z3} = A_1 + A_2 + A_3 \tag{16a}$$

$$B_{z3} = B_1 + B_2 + B_3 \tag{16b}$$

2.3 Solution of the penetration process

(1) Cratering phase

Based on the Newton's second law, and with the initial conditions, z_1 (t = 0) = 0 and V (t = 0) = V_0, the solutions for the displacement, velocity, and acceleration of the ECDP are obtained as shown in Eq. (17).

$$z_1 = \left(\frac{V_0}{\omega}\right)\sin\omega_1 t, 0 \le z_1 \le kd \tag{17a}$$

$$V = \frac{\mathrm{d}z_1}{\mathrm{d}t} = V_0\cos\omega_1 t, 0 \le z_1 \le kd \tag{17b}$$

$$\frac{\mathrm{d}V}{\mathrm{d}t} = \frac{\mathrm{d}^2 z_1}{\mathrm{dt}^2} = -\omega_1 V_0\sin\omega_1 t, 0 \le z_1 \le kd \tag{17c}$$

In Eq. (17), $\omega_1 = (c_1 / m)^{1/2}$.

The time at the end of the cratering phase is defined as t_1. The unknowns t_1, V_1, and c_1 are obtained from the continuity conditions of the axial resistance, velocity, and displacement at $z_1 = kd$ and $t = t_1$. They are expressed as given in Eq. (18).

$$t_1 = \frac{\cos^{-1}\left(V_1/V_0\right)}{\left(c_1/m\right)^{1/2}} \tag{18a}$$

$$V_1 = \sqrt{\frac{V_0^2 - A_d kd/m}{1 + B_d kd/m}} \tag{18b}$$

$$c_1 = \frac{m\left(V_0^2 - V_1^2\right)}{\left(kd\right)^2} \tag{18c}$$

(2) Partial penetration phase

The penetration depth in the partial penetration phase is found from Eq. (19).

$$m\frac{\mathrm{d}^2 z_1}{\mathrm{d}t^2} = -\left[F_{ze} + c_2\left(z_1 - kd\right)\right],\ kd < z_1 \le z_{\mathrm{Pe}} \tag{19}$$

In Eq. (19), z_{Pe} represents the displacement at the end of the partial penetration phase, i.e. $z_{\mathrm{Pe}} = l_A + l_B + l_C + kd$.

Based on the Newton's second law, and with the initial conditions, z_1 ($t = t_1$) = kd and V ($t = t_1$) = V_1, the solutions for the displacement, velocity, and acceleration of the ECDP are obtained as shown in Eq. (20).

$$z_1 = N_1\cos\omega_2 t + N_2\sin\omega_2 t - \left(\frac{F_{ze}}{c_2} - kd\right), kd < z_1 \le z_{\mathrm{Pe}} \tag{20a}$$

$$V = \frac{\mathrm{d}z_1}{\mathrm{d}t} = -N_1\omega_2\sin\omega_2 t + N_2\omega_2\cos\omega_2 t, kd < z_1 \le z_{\mathrm{Pe}} \tag{20b}$$

$$\frac{\mathrm{d}V}{\mathrm{d}t} = \frac{\mathrm{d}^2 z_1}{\mathrm{d}t^2} = -N_1\omega_2^2\cos\omega_2 t - N_2\omega_2^2\sin\omega_2 t, kd < z_1 \le z_{\mathrm{Pe}} \tag{20c}$$

In Eq. (20),

$$\omega_2 = \sqrt{c_2/m} \tag{21a}$$

$$N_1 = \frac{F_{ze}}{c_2}\cos\omega_2 t_1 - \frac{V_1}{\omega_2}\sin\omega_2 t_1 \tag{21b}$$

$$N_2 = \frac{F_{ze}}{c_2}\sin\omega_2 t_1 + \frac{V_1}{\omega_2}\cos\omega_2 t_1 \tag{21c}$$

Further, V_2 and t_2 is defined as the velocity and time of the ECDP at the end of the partial penetration phase, respectively. According to the continuity conditions of the axial resistance, velocity, and displacement at $z_1 = z_{\mathrm{Pe}}$ and $t = t_2$, Eq. (22) is obtained.

$$m\left(N_1\omega_2^2\cos\omega_2 t_2 + N_2\omega_2^2\sin\omega_2 t_2\right) = A_{z3} + B_{z3}V_2^2 \tag{22a}$$

$$-N_1\omega_2 \sin\omega_2 t_2 + N_2\omega_2 \cos\omega_2 t_2 = V_2 \tag{22b}$$

$$N_1 \cos\omega_2 t_2 + N_2 \sin\omega_2 t_2 - \frac{F_{ze}}{c_2} = l_A + l_B + l_C \tag{22c}$$

From Eqs. (22b) and (22c), the following equations are obtained.

$$t_2 = \frac{\sin^{-1}\dfrac{l_A + l_B + l_C + F_{ze}/c_2}{\sqrt{N_1^2 + N_2^2}} - \sin^{-1}\dfrac{N_1}{\sqrt{N_1^2 + N_2^2}}}{\left(c_2/m\right)^{1/2}} \tag{23a}$$

$$c_2 = \frac{m\left(V_1^2 - V_2^2\right) - 2F_{ze}\left(l_A + l_B + l_C\right)}{\left(l_A + l_B + l_C\right)^2} \tag{23b}$$

Further, by Substituting Eq. (22c) into Eq. (22a) yields Eq. (24).

$$c_2 = \frac{A_{z3} + B_{z3}V_2^2 - F_{ze}}{l_A + l_B + l_C} \tag{24}$$

From Eqs. (23b) and (24), Eq. (25) is obtained.

$$\left(B_{z3} + \frac{m}{l_A + l_B + l_C}\right)V_2^2 - \left(\frac{m}{l_A + l_B + l_C}V_1^2 - A_{z3} - F_{ze}\right) = 0 \tag{25}$$

Furthermore, Eq. (25) is solved in order to obtain V_2 and given as shown in Eq. (26).

$$V_2 = \sqrt{\left(\frac{m}{l_A + l_B + l_C}V_1^2 - A_{z3} - F_{ze}\right)\Big/\left(B_{z3} + \frac{m}{l_A + l_B + l_C}\right)} \tag{26}$$

(3) Complete penetration phase
From Newton's second law, Eq. (27) is obtained.

$$m\frac{\mathrm{d}^2 z_1}{\mathrm{d}t^2} = mV\frac{\mathrm{d}V}{\mathrm{d}z_1} = -\left(A_{z3} + B_{z3}V^2\right) \tag{27}$$

With the initial conditions z_1 ($t = t_2$) = z_{Pe} and V ($t = t_2$) = V_2, the following solutions for the displacement, velocity, and acceleration of the ECDP are obtained.

$$z_1(t) = \frac{m}{B_{z3}}\ln\left\{\frac{\cos\left[\tan^{-1}\left(\sqrt{\dfrac{B_{z3}}{A_{z3}}}V_2\right) - \dfrac{\sqrt{A_{z3}B_{z3}}}{m}\left(t - t_2\right)\right]}{\cos\left[\tan^{-1}\left(\sqrt{\dfrac{B_{z3}}{A_{z3}}}V_2\right)\right]}\right\} + z_{Pe}, z_{Pe} < z_1 \le H^* \tag{28a}$$

$$V\left(t\right)=\sqrt{\frac{A_{z3}}{B_{z3}}}\tan\left[\tan^{-1}\left(\sqrt{\frac{B_{z3}}{A_{z3}}}V_2\right)-\frac{\sqrt{A_{z3}B_{z3}}}{m}\left(t-t_2\right)\right],z_{\mathrm{Pe}}<z_1\le H^* \tag{28b}$$

$$\frac{\mathrm{d}V\left(t\right)}{\mathrm{d}t}=-\frac{A_{z3}}{M\cos^2\left[\tan^{-1}\left(\sqrt{\frac{B_{z3}}{A_{z3}}}V_2\right)-\frac{\sqrt{A_{z3}B_{z3}}}{m}\left(t-t_2\right)\right]},z_{\mathrm{Pe}}<z_1\le H^* \tag{28c}$$

The semi-infinite penetration depth is given in Eq. (29).

$$H^*=\frac{m}{2B_{z3}}\ln\left(1+\frac{B_{z3}}{A_{z3}}V_2^2\right)+z_{\mathrm{Pe}} \tag{29}$$

The total penetration time is given in Eq. (30).

$$t_3=\frac{m}{\sqrt{A_{z3}B_{z3}}}\tan^{-1}\left(\sqrt{\frac{B_{z3}}{A_{z3}}}V_2\right)+t_2 \tag{30}$$

3 EXPERIMENT

The ECDP was launched by a 130 mm gas-gun to impact the plain concrete target at the nominal striking velocity of 650 m/s. The experimental result such as the penetration depth of the ECDPs and the failure characteristic parameter of the targets was carefully recorded.

3.1 ECDP and sabot

The dimensions of three ECDPs with a nominal mass of 2.0 kg are shown in Figure 3a and 3b. The major axis and minor axis of the tail ellipse were 72 mm and 48 mm, respectively, the major axis and minor axis of the middle ellipse were 62.4 mm and 41.6 mm, respectively, the length of the double-ogive-nose was 81 mm, and the total length of the ECDP was 208 mm. The interior cavity was filled by the mixture of fine sand and paraffin in order to substitute the filled charge which has a density of 1.8 ± 0.05 kg/m^3. It is worth pointing out that, the ECDPs were designed with equal diameter–thickness ratio, and the diameter–thickness ratio of E1 and E2 was 12 and 16, respectively, so the shell of E1-1 and E1-2 was thicker than that of E2-1. As the diameter of the barrel was larger than the largest major axis of the ECDP, the sub-caliber launch technology was adopted, and the ECDP was equipped with a set of nylon sabot that fit snugly into the barrel. In order to minimize the influence of the sabot on the terminal ballistic effect of the ECDP, the weight reduction design was adopted, and the nominal mass of the sabot was 2.0 kg. Figure 3c shows the separated ECDPs and sabots, and the assembling process. The separated ECDPs and sabots were cleaned using alcohol before the assembly. In order to ensure the integrity of the ECDP and sabot in the barrel, the front sabot and back sabot were glued to the ECDP.

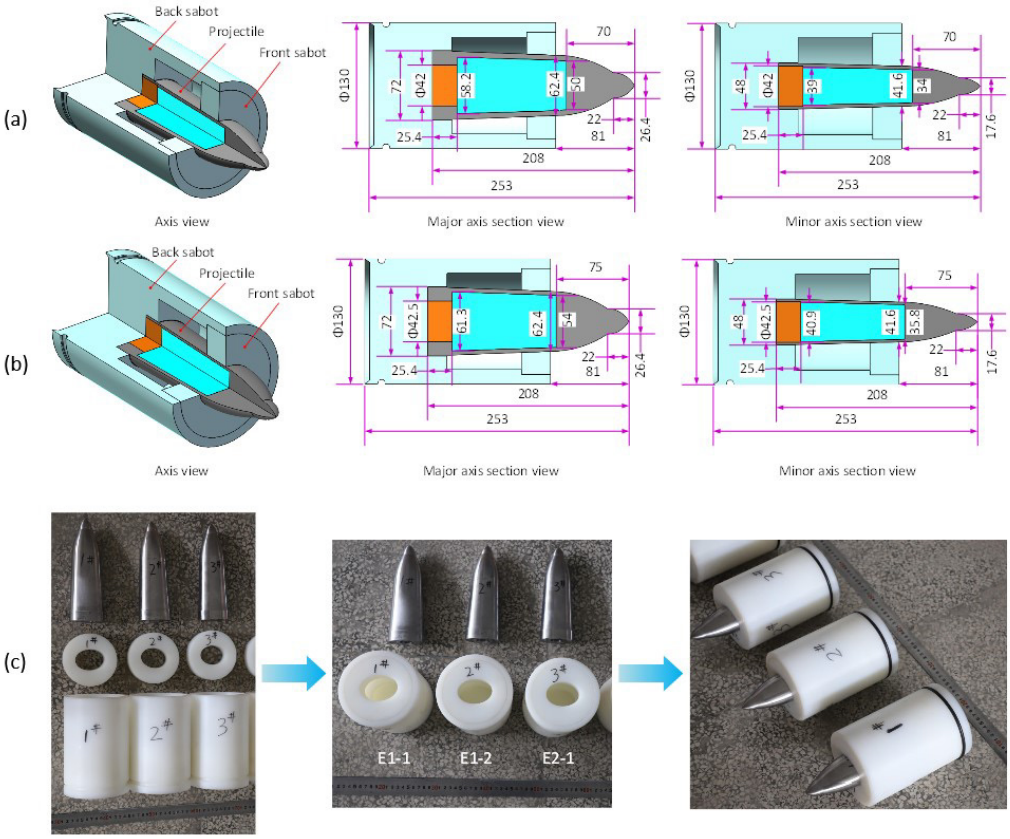

Figure 3 ECDPs and sabots: (a) dimensions of E1-1 and E1-2, (b) dimensions of E2-1, and (c) photographs (Unit-mm).

The ECDPs were machined from the 30CrMnSiNi2MoVE round stock which has a density of 7850 kg/m^3. The 30CrMnSiNi2MoVE steel is a kind of low-alloy high-strength steel, which has high strength, hardenability, and toughness after heat treatment. Standard specimens were machined and tied to the ECDPs during heat treatment, thus the mechanical properties of the ECDPs can be obtained by conducting mechanical tests. Figure 4a shows the quasi-static stress-strain curve that was obtained from the uniaxial tension test, and Figure 4b and 4c show the impacting test and the fracture toughness test, respectively.

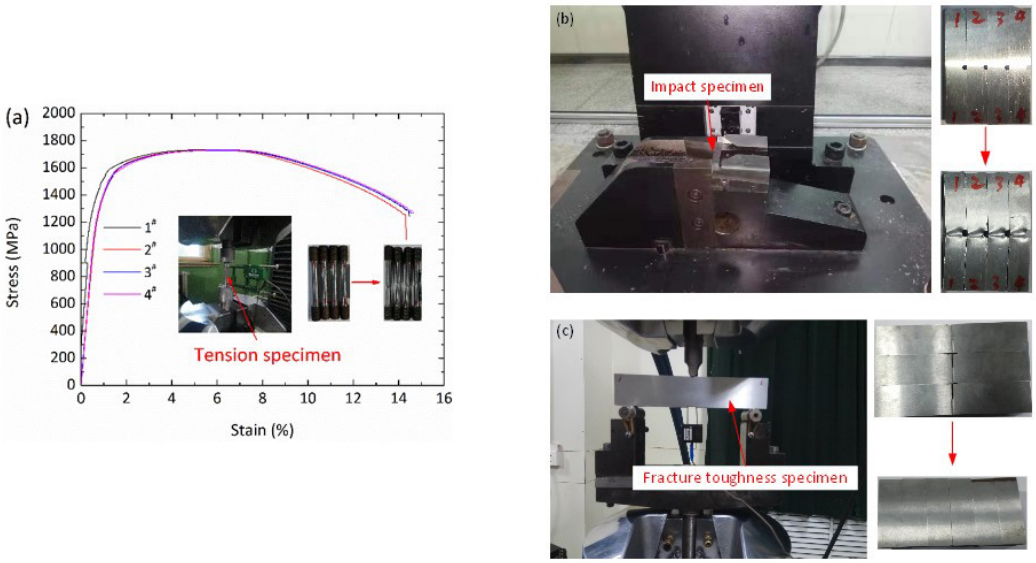

Figure 4 Mechanical tests of the specimens: (a) tension, (b) impact, and (c) fracture toughness.

The mechanical properties of the standard specimens are summarized in Table 1, which includes the yield strength $\sigma_{p0.2}$, fracture strength σ_m, elongation percentage δ_5, contraction of cross-section area ψ_c, impact energy A_{KU2}, and fracture toughness K_{IC}. It is observed that the test results of different standard specimens are consistent. The average of yield strength, impact energy, and fracture toughness are 1350.3 MPa, 59.1 J, and 81.9 MPa·$m^{1/2}$, respectively.

Table 1 Mechanical properties of the standard specimens.

$\sigma_{p0.2}$ (MPa)	σ_m (MPa)	δ_5 (%)	ψ_c (%)	A_{KU2} (J)	K_{IC} (MPa·$m^{1/2}$)
1360	1735	13.5	54	60.5	80.4
1355	1730	13.5	55	56.1	83.0
1345	1730	14.0	54	56.6	82.3
1341	1732	13.5	54	63.1	-

3.2. Target

Three plain concrete targets were cast before the experiment. The target material was the C35 concrete, and the aggregate was fine gravel with diameters ranging between 5 mm and 10 mm. As shown in Figure 5, the dimensions of the target were Φ1200 mm × 1000 mm, the oblique angle was 10°, and the wet density was 2450 kg/m^3. The outer-side of the target was confined by a 6-mm-thick steel hoop to reduce the circumferential boundary effect. In order to obtain the physical property of the plain concrete targets, six standard specimens with 150-mm-length cube were cast and tested, and they exhibited an average unconfined compressive strength of 32.5 MPa.

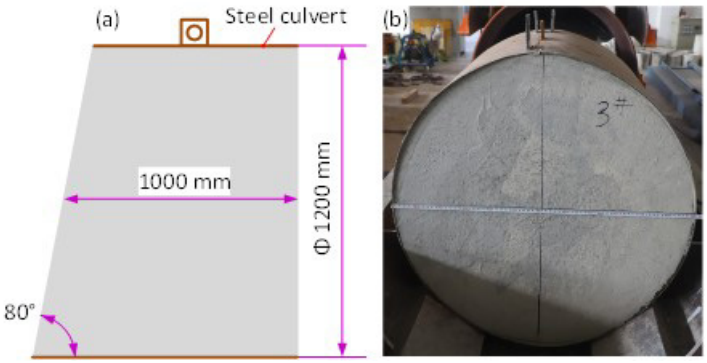

Figure 5 Plain concrete target: (a) a sketch, and (b) a photograph.

3.3. Setup

Figure 6 shows the set-up of the penetration experiment. A 130 mm gas-gun was used to launched the ECDP to impact the concrete target at a nominal striking velocity of 650 m/s. The high-pressure helium gas was increased to 20 MPa by the compressor and then injected into the gas chamber. The fast-acting electromagnetic valve was used to release the high-pressure helium gas into the barrel, and the ECDP was accelerated to impact the target. At the end of the barrel, three laser diodes were separated by a distance of 30 mm and connected to an oscilloscope, which was used for measuring the time the ECDP passed through the laser diodes. Thereafter, the distance between two laser diodes was divided using the travel time, and the striking velocity of the ECDP was calculated. A high-speed camera system was placed in front of the target to record the impacting process. It is worth pointing out that, in order to study the influence of initial posture of the ECDP on the terminal ballistic, when the ECDP was inserted into the barrel, the ECDPs E1-1 and E2-1 were adopted the upright posture, namely, the major axis plane was coincident with the symmetry plane of the target, while the ECDP E1-2 was adopted the lying posture, namely, the minor axis plane was coincident with the symmetry plane of the target.

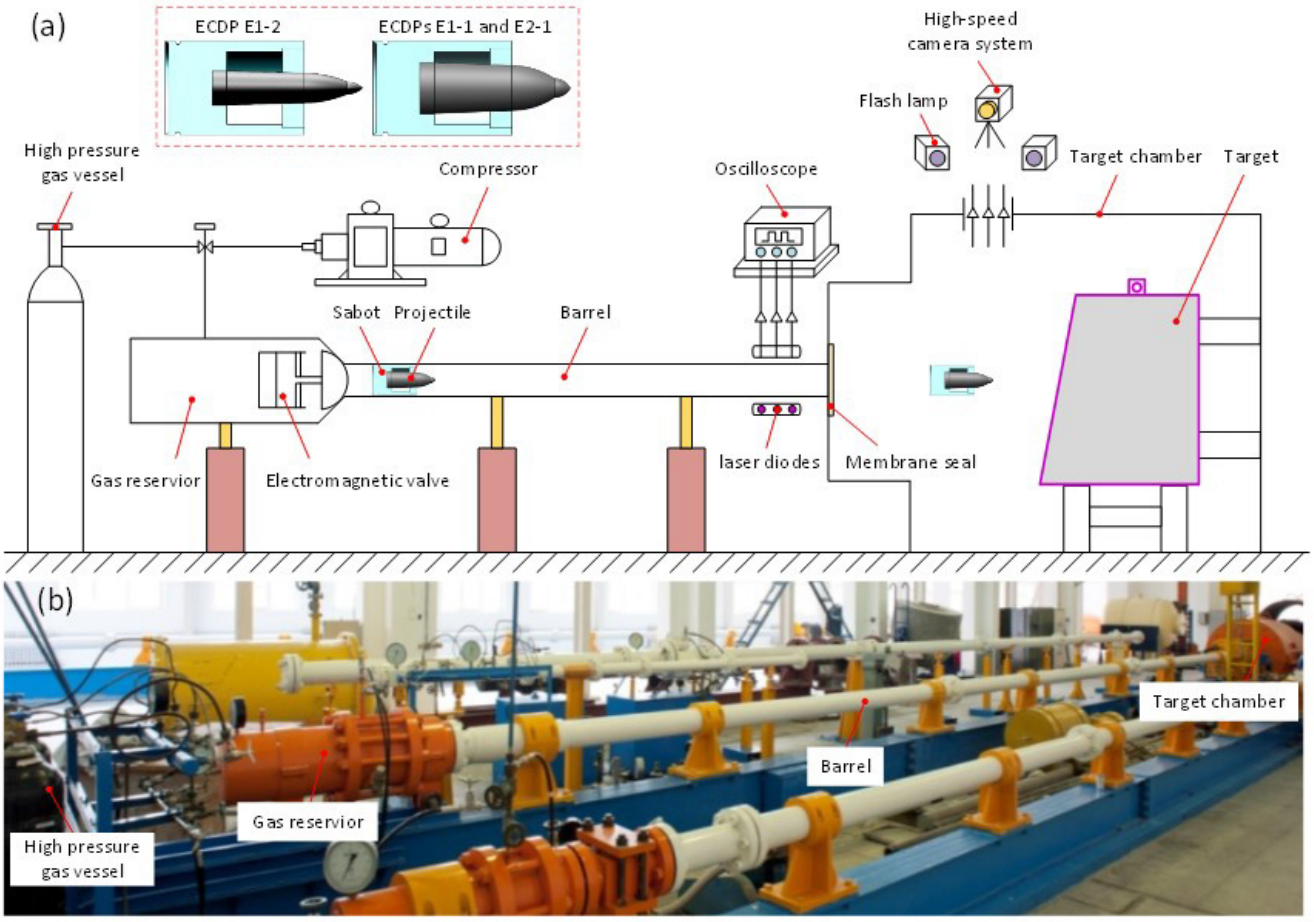

Figure 6 Set-up of the penetration experiment: (a) a sketch, and (b) a photograph.

Figure 7 shows the impacting process of the ECDPs E1-1 and E1-2 was imaged by the high-speed camera system. The flight attitude of the ECDPs almost horizontally, and the pitch angles are negligible. The nylon sabot impacts the target together with the ECDP, but it quickly disintegrated into fragments at the moment of impacting the target.

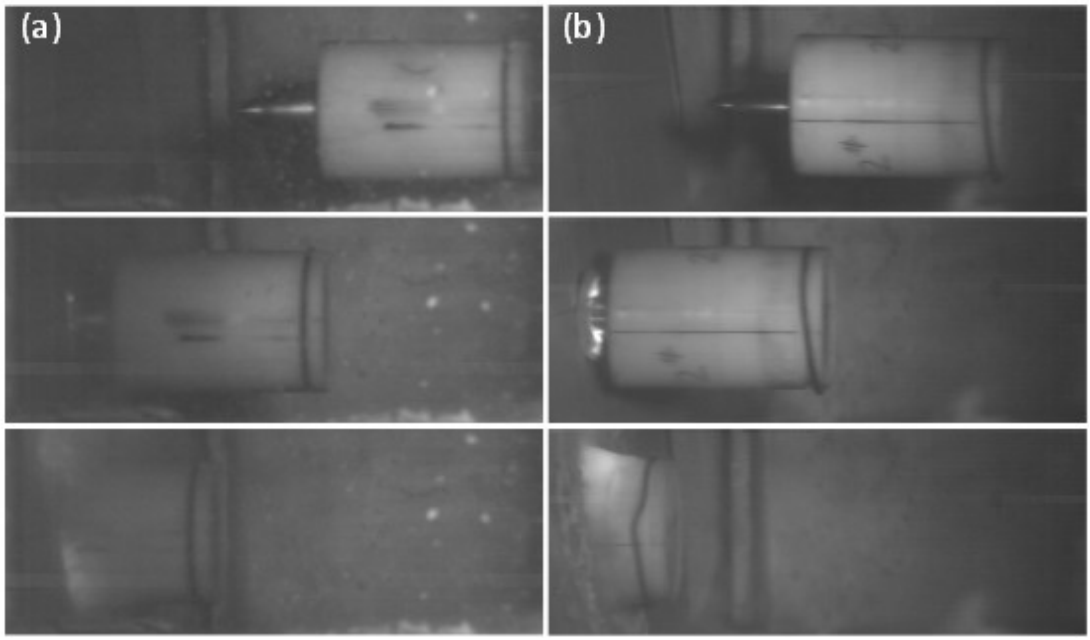

Figure 7 Typical photographs during the impacting process: (a) ECDP E1-1, (b) ECDP E1-2.

3.4. Experimental results

The experimental data, which include the striking velocity V_0, penetration depth H^*, mass m, residual mass m_r, and relative mass loss δ are listed in Table 2. The δ is calculated as $\delta = (m - m_r) / m \times 100\%$, which does not exceed 2.51% for the ECDPs. The striking velocity is controlled at about 650 m/s, and the penetration depth is within the range of 0.473 m ~ 0.518 m.

Table 2 Experimental data.

Shot no.	ECDP type	Initial posture	V_0 (m·s^{-1})	H^* (m)	M (kg)	m_r (kg)	Δ (%)
1	E1-1	upright	663.3	0.473	1.99	1.95	2.01
2	E1-2	lying	678.8	0.518	1.99	1.94	2.51
3	E2-1	upright	672.6	0.498	1.94	1.90	2.06

3.4.1. Recovered ECDP

Figure 8 shows the photograph of the recovered ECDPs. The typical structural responses such as the abrasion, necking, and tensile crack appears in the ECDPs. At a position about 80 mm away from the projectile nose tip which corresponds to the front of the inner cavity, all the ECDPs exhibit slight necking. At a position about 30 mm away from the projectile tail which corresponds to the tail of the inner cavity, ECDP E1-1 only exhibits significant necking, ECDP E1-2 exhibits significant necking on one side and exhibits tensile crack on the other side, and ECDP E2-1 exhibits significant tensile crack on both sides. Further, both necking and tensile crack occur near the minor axis, as shown in the white dotted frame. This is because the ECDPs are adopted the design of the equal diameter–thickness ratio, the absolute wall thickness is not uniformly distributed and increases gradually along the circumference from the minor axis to the major axis. Therefore, at the sudden changes in the cross section of the ECDPs, under the action of the incident compression wave and the reflected tensile wave, the stress at the place with the thinnest wall which corresponds to the minor axis, is the largest, so the necking deformation and tensile crack initially start from here, and gradually expand and then decrease along the circumference to the major axis. Eventually, almost no necking deformation is observed near the major axis.

Figure 8 Photographs of the recovered ECDPs: (a) front view, (b) rear view, (c) side view, (d) Enlarged view of tensile crack, and (e) Enlarged view of necking.

From Figure 8, it is also observed that the necking in the ECDP E1-2 is more obvious than that in the ECDP E1-1, and the structural response on the upper and lower surfaces are different. This is because, the target had an oblique angle, the force on the lower surface of the ECDP was greater than that on the upper surface, thus the deflection bending moment was generated under the action of the asymmetric force of the target. Meanwhile, the ECDP E1-2 impacts the target in a lying posture, the projected area on the target surface is larger, so the deflection bending moment is also greater, ultimately resulting in a more pronounced asymmetric structural response relative to ECDP E1-1.

3.4.2. Damage of the target

Figure 9 shows the damage of the targets after experiment. The weld of the steel hoops was torn during the penetration process, 11 ~ 14 radial cracks were observed, and they propagated to the border on the front surface of the targets. The dimensions of the initial hole of the tunnel are larger than the major axis of the ECDP, and some fragments of the nylon sabot were found in the tunnel. Therefore, it can be inferred that the nylon sabot may follow the projectile to a distance and has some influence on the terminal ballistic effect of the projectile. As discussed in Rosenberg and Kositski (2016), when the projectile reached a distance of about 3.5*d* from the rear surface of the concrete target, it starts to affect the resistance stress on the projectile. In the present experiments, the ECDPs stopped where the distance from the rear surface was at least 482 mm, which was greater than 3.5 times the major axis of the tail ellipse. Therefore, the rear-surface effect can be ignored.

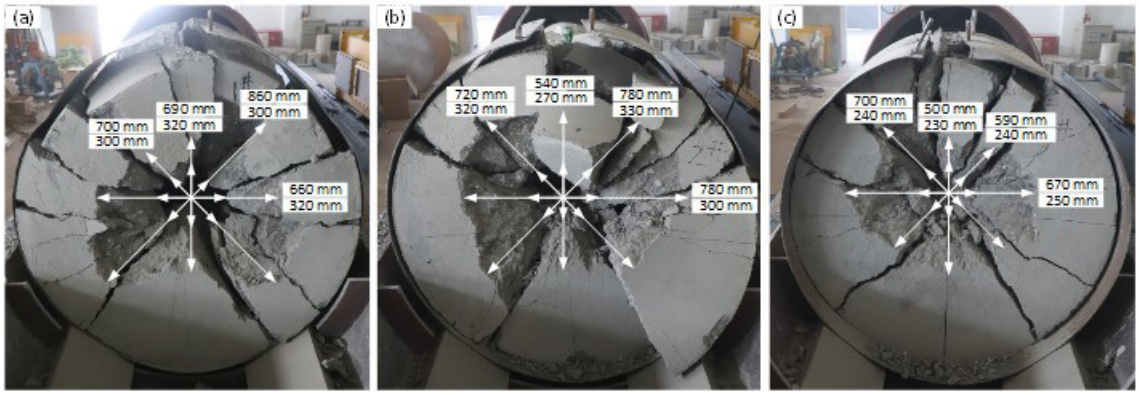

Figure 9 Damage of targets: (a) no. 1, (b) no. 2, and (c) no. 3.

According to the damage of targets and referring to the definition of penetration model in Wu et al. (2012), Chen et al. (2008), and Peng et al. (2015), the two-stage (front cater + tunnel) damage model of the target was proposed, as shown in Figure 10. D_h, D_1, D_v, and D_2 represent the maximal dimensions of the front crater in four directions: horizontal, 45°, vertical, 135°, respectively. d_h, d_1, d_v, and d_2 represent the maximal dimensions of the initial hole of the tunnel in four directions: horizontal, 45°, vertical, 135°, respectively. H_f and H_t represent the front crater depth and tunnel depth, respectively. β represents the trajectory deflection angle in the vertical plane, which is the angle between the straight line from the impact-point to the end-point and the horizontal line.

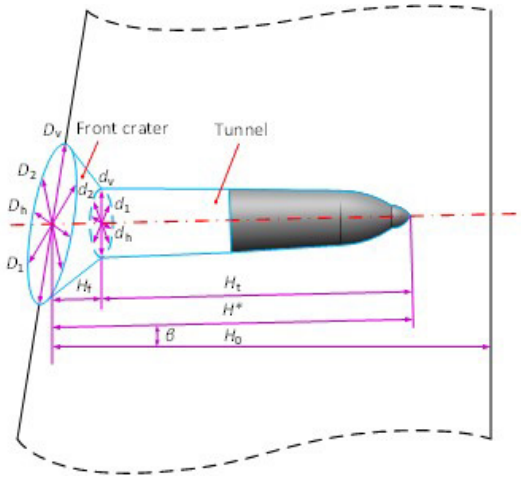

Figure 10 Schematic diagram of two-stage damage model of the target.

Table 3 lists the failure characteristic parameters of the targets. The size of the damage area on the front surface is between 500 mm and 860 mm, the size of the initial hole of the tunnel is between 230 mm and 330 mm, and the front crater depth is between 150 mm and 210 mm. Due to the serious cracking of the target, the trajectory preservation is not very complete, and it can only be judged that the trajectory is basically not deflected.

Table 3 The failure characteristic parameters of the targets.

Shot no.	ECDP type	D_h(mm)	D_1(mm)	D_v(mm)	D_2(mm)	d_h(mm)	d_1(mm)	d_v(mm)	d_2(mm)	H_f(mm)
1	E1-1	660	860	690	700	320	300	320	300	210
2	E1-2	780	780	540	720	300	330	270	320	150
3	E2-1	670	590	500	700	250	240	230	240	170

3.4.3. Penetration depth

Figure 11 shows a comparison of penetration depth of the ECDPs. The penetration depth is positively correlated with the projectile velocity, and which is very close whether the ECDP adopts the upright posture or the lying posture, indicating that the initial posture has little effect on the penetration depth under the condition of the target with 10° oblique angle.

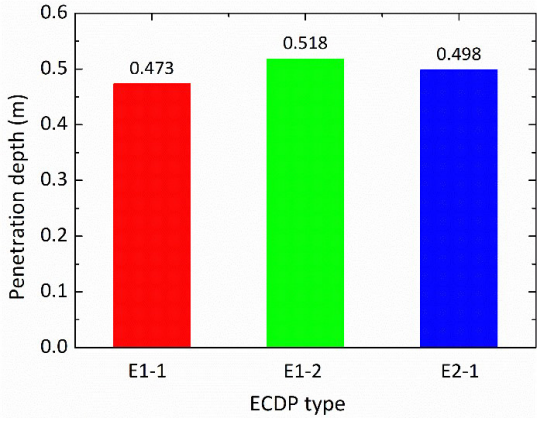

Figure 11 Comparison of penetration depth.

4 VALIDATION OF THEORETICAL MODEL AND DISCUSSION

Since the ballistic deflection of the ECDP is small during the penetration process, it can be considered that the penetration depth of the ECDP under the 10° oblique penetration condition is almost the same as that under the normal penetration condition. Therefore, it is reasonable and reliable to verify the theoretical model using the experimental data of penetration depth.

Figure 12 to Figure 15 show the deceleration and velocity with respect to time and displacement of the ECDP calculated by the theoretical model. The deceleration change is divided into three phases. In the cratering phase, the deceleration increases rapidly. In the partial penetration phase, the deceleration increases slowly. In the complete penetration phase, the deceleration gradually decreases and plummets to zero. The maximum peak deceleration is close to 600,00 g (g = 9.81 m/s^2). The velocity decreases almost linearly, and eventually drops to zero. The law of deceleration and velocity evolution is consistent with the conventional understanding.

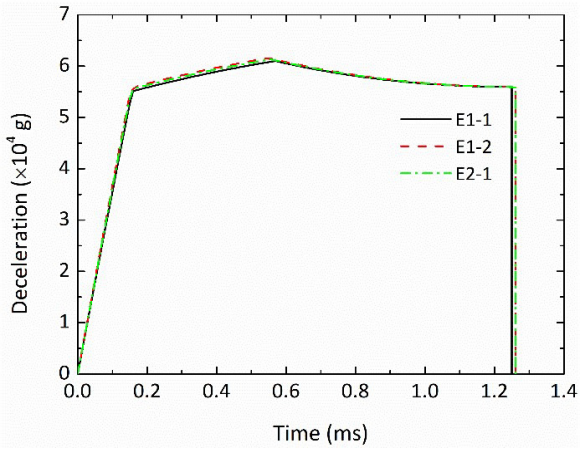

Figure 12 Deceleration versus time of the ECDP.

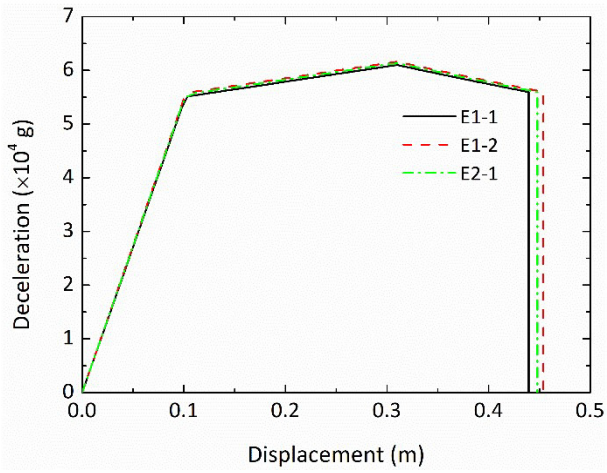

Figure 13 Deceleration versus displacement of the ECDP.

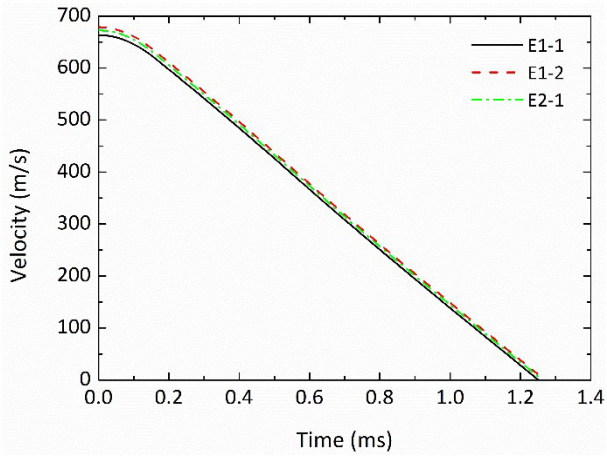

Figure 14 Velocity versus time of the ECDP.

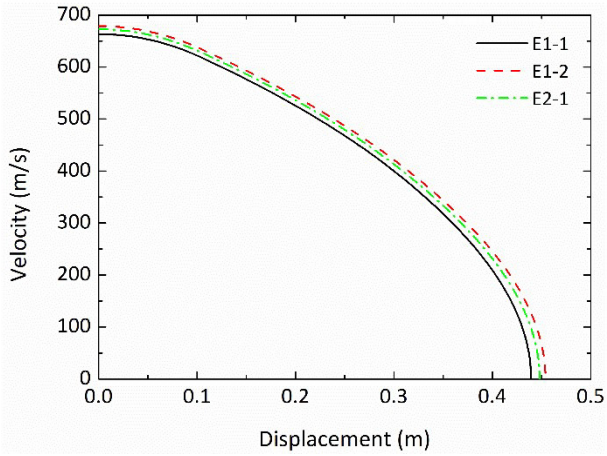

Figure 15 Velocity versus displacement of the ECDP.

Figure 16 shows a comparison between the calculated result of the penetration depth using the proposed model and the experimental data. The calculated result is in good agreement with the experimental data, and the deviation is within the range of -13.5% ~ -8.5%. There are two main sources of the deviation. First, the insufficient circumferential constraint of the target result in the side boundary effect, thus the penetration resistance of the ECDP was smaller than that in the ideal situation of the semi-infinite penetration, this may increase the penetration depth of the ECDP. Second, the nylon sabot impacts the target together with the ECDP, even though part of it is rapidly fragmented at the moment of impacting, the rest follows the ECDP for a long distance as an additional mass, which may also increase the penetration

depth to some extent. Therefore, if not for the above two important factors, the actual penetration depth of the ECDP will be reduced, and the calculation accuracy of the theoretical model will be higher.

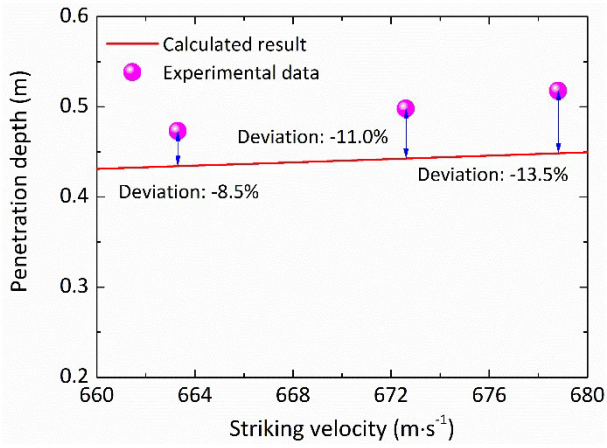

Figure 16 Comparison of the calculated result and the experimental data.

5 CONCLUSIONS

In this work, the theoretical model of the ECDP penetration into semi-infinite plain concrete target was proposed, the experiment of the ECDP penetration into plain concrete target was performed, and the theoretical model was verified by experimental data. The main work and conclusions are as follows:

(1) The general geometric model of the ECDP was established, and the expression of penetration resistance was obtained by integrating the resistance stress on the surface of the ECDP. Based on the special shape and penetration process characteristics of the ECDP, a three-stage penetration model was constructed. By solving the kinematics of the penetration process, the analytical solution of the terminal ballistic parameters of the ECDP was obtained.

(2) The experimental data such as the penetration depth of the ECDPs and the failure characteristic parameter of the targets was obtained. The penetration depth was within the range of 0.473 m ~ 0.518 m at a nominal striking velocity of 650 m/s, the size of the damage area on the front surface was between 500 mm and 860 mm, and the front crater depth was between 150 mm and 210 mm.

(3) The initial posture of the ECDP had little effect on the penetration depth and trajectory deflection under the condition of the target with 10° oblique angle, but it had obvious influence on the structural response. The asymmetric structural response of the ECDP E1-2 in the lying posture was more obvious than that of the ECDP E1-1 in the upright posture.

(4) The calculated result of the penetration depth by the theoretical model was in good agreement with the experimental data, the deviation was within the range of -13.5% ~ -8.5%, and the deviation mainly comes from the side boundary effect and nylon sabot. Therefore, more ideal experiments are needed to be conducted to further verify the validity of the theoretical model in the future.

Author's Contributions: Conceptualization, KH Wang and G Zhou; Methodology, XH Dai; Validation, XH Dai, ZK Shen and M Li; Formal analysis, M Ke; Investigation, KH Wang; Resources, G Zhou; Data curation, XH Dai; Writing—original draft preparation, XH Dai; Writing—review and editing, KH Wang; Supervision, G Zhou.

Editor: Rogério José Marczak

References

Chen X.W., Li X.L., Huang F.L., Wu H.J., Chen Y.Z. (2008). Normal perforation of reinforced concrete target by rigid projectile. Int J Impact Eng 35:1119-1129.

Dai X.H., Wang K.H., Duan J., Li M.R., Qian B.W., Zhou G. (2020). A rigid elliptical cross-sectional projectile with different geometrical characteristics penetration into concrete target. Journal of Physics: Conference Series, 1507 032001.

Dai, X.H., Wang K.H., Li M.R., Duan J., Qian B.W., Zhuo G. (2021). Rigid elliptical cross-section ogive-nose projectiles penetration into concrete targets. Def Technol 17:800-811.

Dong H., Liu Z.H., Wu H.J., Gao X.D., Pi A.G., Huang F.L. (2019). Study on penetration characteristics of high-speed elliptical cross-sectional projectiles into concrete. Int J Impact Eng 132:1-12.

Forrestal M.J., Altman B.S., Cargile J.D. (1994). An empirical equation for penetration depth of ogive-nose projectiles into concrete targets. Int J Impact Eng 15:395-405.

Frew D.J., Hanchak S.J., Green M.L., Forrestal M.J. (1998). Penetration of concrete targets with ogive-nose steel rods. Int J Impact Eng 21:489-497.

Li Q.M., Chen X.W. (2003). Dimensionless formulae for penetration depth of concrete target impacted by a rigid projectile. Int J Impact Eng 28:93-116.

Liu J.C., Pi A.G., Huang F.L. (2015). Penetration performance of double-ogive-nose projectiles. Int J Impact Eng 84:13-23.

Peng Y., Wu H., Fang Q., Gong Z.M., Kong X.Z. (2015). A note on the deep penetration and perforation of hard projectiles into thick targets. Int J Impact Eng 85:37-44.

Rosenberg Z., Kositski R. (2016). Modeling the penetration and perforation of concrete targets by rigid projectiles. Int J Protective Struct 7:157-178.

Sun C.J., Lu Y.G., Zhang F.J., Li H.M. (2010). Penetration of cylindrical-nose-tip projectiles into concrete targets. Explosion and Shock Waves 30:269-275.

Teland J.A., Sjol H. (2004). Penetration into concrete by truncated projectiles. Int J Impact Eng 30:447-464.

Wu H., Fang Q., Zhang Y.D., Gong Z.M. (2012). Semi-theoretical analyses of the concrete plate perforated by a rigid projectile. Acta Mechanica Sinica 28:122-135.

Wu H.J., Deng X.M., Dong H., Tian Z., Yang G.X., Huang F.L. (2023). Three-dimensional trajectory prediction and analysis of elliptical projectile. Int J Impact Eng 74:104497.

Zhang S., Wu H.J., Zhang X.X., Liu J.C., Huang F.L. (2017). High-velocity Penetration of Concrete Targets with Three Types of Projectiles: Experiments and Analysis. Latin American Journal of Solids and Structures 14:1614-1628.